Title: **Critical Progressive Damage Analysis Model Features for Low-Velocity Impact on Thermoset and Thermoplastic Panels**

Authors: Frank Leone
Wade Jackson
Cheryl Rose
Banavara Seshadri

ABSTRACT

A previous verification and validation framework evaluated the ability of various progressive damage analysis (PDA) tools to predict the mechanical response and damage state in post-buckled stiffened aerospace structures composed of fiber-reinforced thermoset composite materials. Herein, the ability of PDA tools to predict damage in thermoplastic composite materials subject to low-velocity impact (LVI) loading has been assessed. LVI tests and analyses have been conducted for similar panels, comprising thermoset or thermoplastic composite materials. Preliminary test/analysis correlations revealed that using the same combination of PDA model features and finite element model-building guidelines for the thermoset and thermoplastic LVI specimens resulted in underprediction of matrix crack lengths and delaminated area in the thermoplastic analyses despite yielding good correlations for the thermoset specimens. In this paper, the quality of the test/analysis correlations for analyses of thermoplastic LVI specimens performed with different combinations of PDA model features using the NASA CompDam material model are presented. Model features that were assessed in terms of effect on the quality of the test/analysis correlation include the representation of damageable interfaces, residual thermal stresses, and fiber damage.

INTRODUCTION

Progressive damage analysis (PDA) tools for fiber-reinforced composite materials have a wide range of representable damage modes, stress/strain nonlinearities, and other complex modeling features. Damage modes that are typically considered include in-plane matrix cracking, interlaminar delaminations, tensile fiber fracture, and fiber kink bands. Nonlinear stress/strain responses can have a variety of shapes, in one or multiple

---

Frank Leone, NASA Langley Research Center, Hampton, Virginia 23681, U.S.A.
Wade Jackson, NASA Langley Research Center, Hampton, Virginia 23681, U.S.A.
Cheryl Rose, NASA Langley Research Center, Hampton, Virginia 23681, U.S.A.
Banavara Seshadri, Analytical Mechanics Associates, Hampton, Virginia 23666, U.S.A.

planes, and can be attributed to either plasticity or micro-scale damage. The initial state of the material can be assumed either to be unloaded and pristine or, conversely, to contain residual stresses from material processing and a distribution of internal voids and defects. Material properties can be assumed to be constant or statistically distributed. Each of these potential model features has its own set of assumptions and limitations that should be verified and validated in isolation and in combination.

In the former NASA Advanced Composites Project (ACP), a verification and validation framework was developed for the application of PDA tools to the prediction of matrix cracks, delaminations, and their interactions in post-buckled aerospace structures [1]. Validation articles included quasi-statically loaded seven-point bend specimens [2], single-stringer compression specimens [3], and four-stringer compression specimens [4]. Damage in the specimens occurred predominantly in a unidirectional fiber-reinforced toughened thermoset epoxy resin material (i.e., IM7/8552). Several PDA tools were exercised, including methods based on continuum damage mechanics (CDM), discrete damage mechanics (e.g., the floating node method [5]), cohesive zone modeling, and the virtual crack closure technique. The test/analysis correlations achieved with each of the evaluated methods were of high quality in terms of the load/displacement histories and the damage morphologies. The overall damage sizes were well-predicted early in the damage evolution histories, though the test/analysis correlation error increased as the damage size increased. The development and application of the verification and validation framework in the NASA ACP yielded a set of best practices for the application of PDA tools to aerospace structures composed of fiber-reinforced composite materials.

The ability of PDA tools to predict damage in thermoplastic composite materials is being assessed as part of the NASA Hi-Rate Composite Airframe Manufacturing (HiCAM) project. Low-velocity impact (LVI) tests and analyses have been conducted for similar panels composed of thermoset or thermoplastic composite materials. Preliminary test/analysis correlations have revealed that using the same combination of PDA model features and finite element model-building guidelines for the thermoset and thermoplastic LVI specimens resulted in worse underprediction of matrix crack lengths and delaminated area in the thermoplastic analyses than in the thermoset analyses. In this paper, the quality of the test/analysis correlations for analyses of thermoplastic LVI specimens performed with different combinations of PDA model features with a CDM-based material model are compared. The model features assessed in terms of effect on the quality of the test/analysis correlation include the representation of damageable interfaces, the inclusion of residual thermal stresses, and the consideration of fiber damage.

EXPERIMENTS

Panels composed of two different material systems were included in this study, one with a thermoset epoxy resin (IM7/8552 from Hexcel Corp.[1]) and one with a thermoplastic resin (APC AS4D/PEKK-FC from Solvay[1]). The thermoset panels had a

---

[1] Specific vendor and manufacturer names are explicitly mentioned only to accurately describe the material studied. The use of vendor and manufacturer names does not imply an endorsement by the U.S. Government, nor does it imply that the specified material is the best available.

16-ply stacking sequence of $[+45_2/0_2/-45_2/90_2]_S$, with a nominal laminate thickness of 0.076 inch. The thermoplastic panels had a 24-ply stacking sequence of $[-45/0/+45/90]_{3S}$, with a nominal laminate thickness of 0.135 inch. The difference in stacking sequence was not deliberate, but a consequence of using panels designed and built for different projects.

All testing was conducted at NASA Langley Research Center (LaRC) in the Materials Research Laboratory. Impact specimens were constrained using a bolted, steel picture frame support during the tests. Two panel dimensions were tested: 14-inch-by-14-inch and 8-inch-by-8-inch. The picture frame support for the 14-inch specimens had a 10-inch-by-10-inch unsupported opening, and the support for the 8-inch specimens had a 5-inch-by-5-inch opening. The support for the 8-inch specimens is shown in Figure 1. The bolt holes in the picture frame supports were located at half the frame width and were evenly spaced around the perimeter. Seven bolts were used to secure each edge of the 14-inch frame, and three bolts were used to secure each edge of the 8-inch frame. The impactor had a steel, hemispherical tup. Tup diameters of 0.5 inch and 1.0 inch were used in different tests. The drop heights of the impactor were selected to yield the desired impact energies. The total mass of the impactor assembly was 3.80 lb_m for all the tests presented in this paper.

Data collected during the LVI tests included force versus time histories from a force transducer in the impactor assembly and displacement versus time at the center point of the panel back side via a fiber-optic sensor. Residual dent depths and profile measurements were performed posttest. Specimens were scanned before and after impact via ultrasonic testing (UT) and posttest via X-ray computed tomography (CT). The UT data were primarily used to identify and measure interlaminar delaminations, and the X-ray CT data were used to identify and measure intralaminar matrix cracks and fiber tow breaks. UT scans were conducted from both the top (impacted) and bottom (back) surfaces in order to characterize delamination damage that would have otherwise been shadowed by damage on other interfaces. A thorough manual segmentation of the matrix crack, delamination, and fiber tow breaks was conducted for select specimens, using the UT and X-ray CT data to make a combined damage map for use in test/analysis correlations [6].

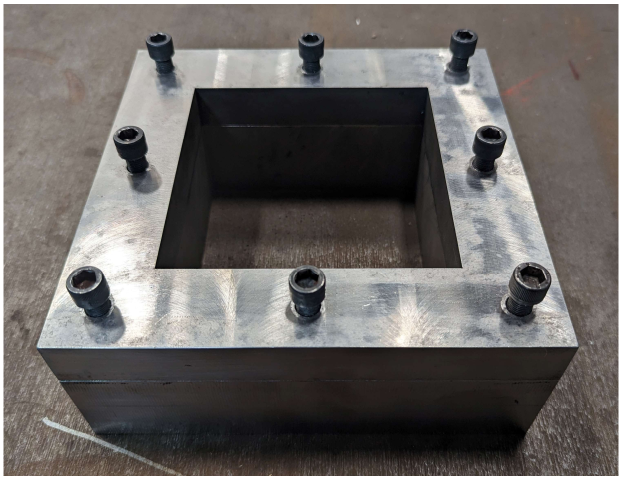

Figure 1. Square, 8-inch LVI picture frame support with a 5-inch-by-5-inch opening.

Impact energies ranging from 2.5 ft-lb$_f$ to 25 ft-lb$_f$ were evaluated in order to generate different combinations of damage modes in the panels composed of the thermoset and thermoplastic material systems. In this paper, the following limited subset of experimental data is featured:

1. A 14-inch thermoset panel, impacted with a 0.5-inch-diameter tup with an impact energy of 3.5 ft-lb$_f$,
2. An 8-inch thermoplastic panel, impacted with a 1.0-inch-diameter tup with an impact energy of 6 ft-lb$_f$, and
3. An 8-inch thermoplastic panel, impacted with a 1.0-inch-diameter tup with an impact energy of 10 ft-lb$_f$.

An example of the manually segmented delamination data for the 10 ft-lb$_f$ impact on the 8-inch thermoplastic panel is shown in Figure 2.

MODELS

The finite element models presented in this paper were initially constructed according to the best practices established in the verification and validation of the NASA CompDam material model [7] conducted during the former NASA ACP. In the prior validation effort, it was found that for CDM-based PDA methods a discrete fiber-aligned, ply-by-ply, interface-by-interface meshing approach produced high-quality results. Each damageable ply was meshed with a single layer of solid elements. The solid-layer meshes were generally orthogonal, with the meshlines parallel and

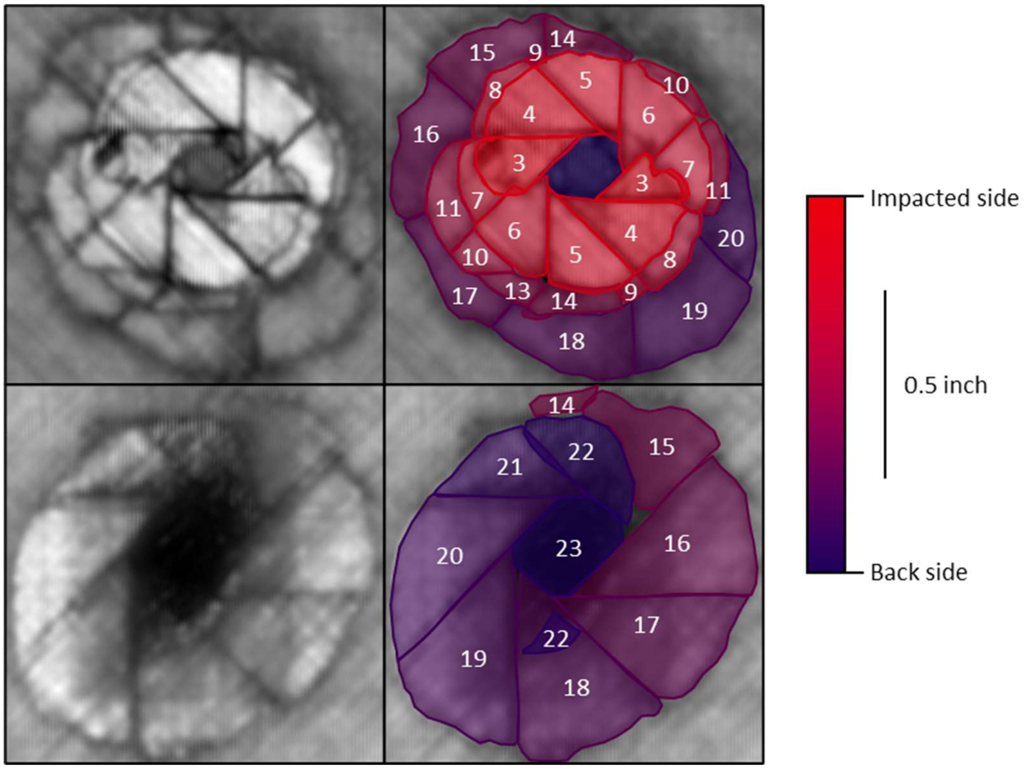

Figure 2. UT amplitude plots (*left*) and labeled delaminations (*right*), as viewed from the impacted (*top*) and back (*bottom*) sides, for a 10 ft-lb$_f$ impact on an 8-inch thermoplastic panel. The interfaces are numbered 1 through 23, impacted side to back side.

perpendicular to the fiber material direction. A minimum matrix crack spacing was enforced to promote crack growth along the fiber direction and to ensure stress concentrations could form ahead of each matrix crack [8]. Each damageable interface was meshed by a single layer of zero-thickness cohesive elements with high, numerical penalty stiffnesses. The alternating layers of solid and cohesive elements were connected via tied constraints. An example of this ply-by-ply, interface-by-interface meshing approach is shown in Figure 3.

The prior work was focused on validating PDA models for application to stiffened, post-buckled structures. The damage in these stiffened, post-buckled structures typically initiated along the edge of the stiffener flange and propagated two to four plies into the skin panel thickness. For the LVI analyses presented herein, damage was expected to propagate through the thickness of the laminate, so each ply and interface of the mesh in the central region of the panel was meshed with the discrete ply-by-ply, interface-by-interface technique. This refined, central region (the yellow region in Figure 4) was sized to contain the expected damage size while maintaining computational tractability.

Material properties for the AS4D/PEKK-FC thermoplastic material system were taken from [9]. Material properties for the IM7/8552 thermoset material system can be found in [2, 3]. No rate-dependent effects were considered for either material system.

The LVI panel boundary conditions consisted of through-thickness constraints on the nodes within the picture frame support and in-plane constraints at the bolt locations, consistent with the recommendation of Song [10]. The outer region of the panel where these boundary conditions were applied (the blue region in Figure 4) consisted of conventional shell elements arranged in a coarse, orthogonal mesh. Shell-to-solid constraints were used to connect the coarsely meshed region to a solid-element transition region (cyan region in Figure 4), which was then tied to the outer edge of the central refined region. The finite element model shown in Figure 4 is for an 8-inch-by-8-inch, 24-ply thermoplastic panel, with a 2-inch-by-2-inch refined region and a 2.5-inch-by-2.5-inch transition region. The element edge lengths were 0.00787 inch in the refined region and 0.375 inch in the coarse region. The element sizes in the refined regions were selected to avoid constitutive snap-back [11] and to satisfy additional fracture-based requirements [12]. The thermoplastic panel models had approximately 18 million degrees of freedom in total.

The impactor was modeled as an analytical rigid surface (green mesh in the center of Figure 4) with a point mass at its center of curvature. The impactor was positioned so that the surfaces of the impactor and the top ply of the refined mesh region were initially in contact. An initial downward velocity was assigned to the reference point of the impactor to control the impact energy. All rotations and the in-plane translations of the impactor were otherwise constrained. Kinematic contact was modeled between the impactor and the top surface of the panel.

A single explicit dynamic load step was used to simulate the impact event. The maximum step duration (10 ms) was selected based on the experimental impact durations. The analyses were automatically terminated if the impactor returned to its initial vertical position prior to reaching the maximum step duration. Mass scaling was used to reduce the minimum stable increment and maintain it at a specified value (8.33 ns) to make the analyses computationally tractable. An element-by-element mass scaling approach was applied at each solution increment, increasing individual elemental masses as necessary to maintain the target time increment. The analyses were solved using Abaqus/Explicit 2021.HF6[1] with 80 cores on the NASA LaRC K4

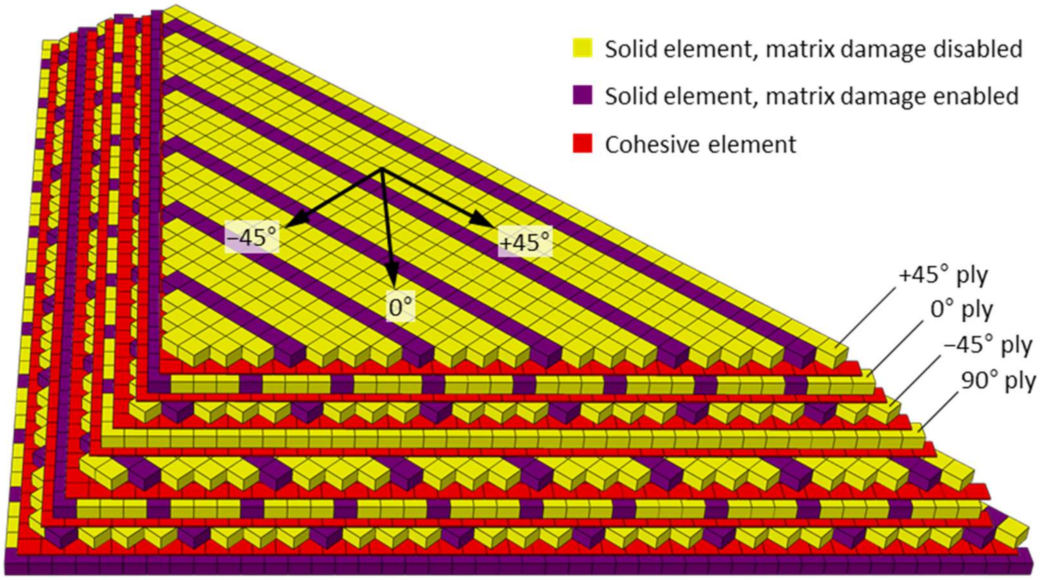

Figure 3. Ply-by-ply, interface-by-interface, fiber-aligned finite element mesh.

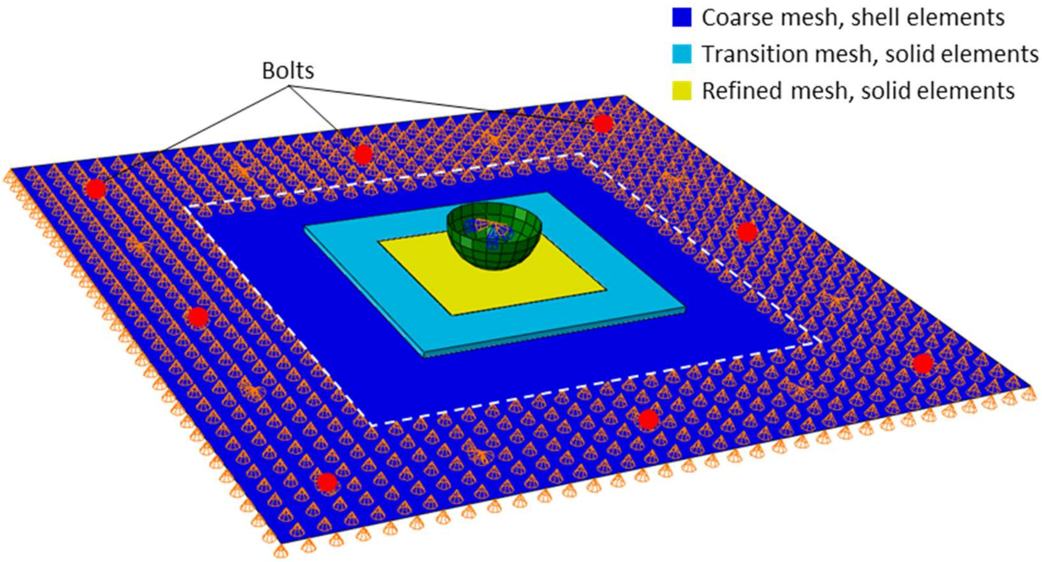

Figure 4. LVI finite element model schematic for an 8-inch panel with a 2-inch-by-2-inch refined region with superposed boundary conditions for the picture frame support.

cluster, described in reference [13]. Analysis run times varied with model size and impact duration, but were generally between 24 hour and 36 hours.

RESULTS

Interface Representation

In the prior verification and validation study, layers of zero-thickness cohesive elements were used to represent the damageable interfaces in laminated composite panels. Experimental loads were applied quasi-statically, so a combination of time- and mass-scaling was used to maintain computational tractability for the explicit finite element analyses. The amount of mass-scaling was selected to maximize the minimum stable time increment while not introducing artificial dynamic effects during loading. For the LVI analyses studied herein, step time was treated as physical time, and time-scaling was not used. As mentioned in the previous section, mass-scaling was applied sparingly in the LVI analyses, though it was required by the explicit finite element solver that additional non-physical mass be assigned to the zero-thickness cohesive elements.

The best practices of the prior approach were first applied to an LVI on a thermoset panel. The experimental and analytical force-time histories for a 3.5 ft-lb$_f$ impact on a 14-inch thermoset panel are represented in Figure 5. The test/analysis correlation of the force-time history (green dash-dot line in Figure 5) was considered to be good—the peak load and impact duration were well captured, and the lesser vibrations of the response agreed in time, though the vibrations in the analysis had larger amplitudes than the experiment. Furthermore, predicted damage size and morphology agreed well with experimental observations. The damage states as measured by UT amplitude plots and as predicted by the analysis with zero-thickness cohesive elements, as viewed from both the impacted and back sides on the panel are depicted in Figure 6.

Having successfully applied the modeling approach to a thermoset panel, the same approach was applied to a 24-ply thermoplastic panel. The experimental and analytical force-time histories for a 10 ft-lb$_f$ impact on an 8-inch thermoplastic panel are represented in Figure 7. While the peak load and impact duration again agreed with the experimental response, a low-frequency, high-amplitude vibration was present throughout the predicted force-time history (green dash-dot line in Figure 7).

Several additional analyses were proposed and performed to identify the cause of the predicted vibrations and explain why the vibrations were much more pronounced in the thermoplastic panel analysis. Models composed of conventional shell elements with elastic material definitions were conducted for both the thermoset (gray dotted line in Figure 5) and thermoplastic (gray dotted line in Figure 7) panels, and it was found that the experimental force-time histories could be accurately predicted prior to the onset of damage with this much simpler model. A series of analyses was then conducted in which model features were disabled or removed from the initial PDA in an attempt to more closely match the experimental force-time history. Investigated model variations included: disabling intralaminar and interlaminar damage predictions within the PDA material model, replacing the PDA material model with a linear-elastic material, and removing the cohesive elements from the mesh. The removal of the cohesive elements altogether produced a force-time history similar to the initial experimental response and the conventional shell element analysis. Because the cohesive elements had a linear-elastic traction-separation law prior to their removal, only their penalty stiffness and mass inputs remained as potential culprits.

To address potential issues associated with both the penalty stiffness and the additional mass associated with the zero-thickness cohesive elements, the LVI model was changed to include finite-thickness cohesive elements. To enable this change, the finite-thickness cohesive element formulation of Sarrado [14] was implemented in CompDam. The cohesive element thickness was set to one-tenth of the nominal ply thickness, and the in-plane material properties of the solid elements were appropriately scaled to accommodate their reduced relative thickness. The cohesive penalty stiffness properties were based on the transverse moduli of the ply material. The force-time histories of the PDA including finite-thickness cohesive elements much more closely agreed with experiments for both the thermoset and thermoplastic cases, the red dashed lines in Figure 5 and Figure 7, respectively.

To further establish the sensitivity of the predicted force-time histories to additional cohesive element mass, a variation of the thermoplastic LVI analysis was run in which the mass of the cohesive elements was set only so high as to avoid additional mass-scaling being required to achieve the specified minimum stable time increment. This lower-mass variation of the analysis increased the total mass of the panel by only 10%; the initial zero-thickness cohesive element analysis roughly doubled the mass of the panel. While reducing the artificial mass associated with the cohesive elements yielded an improvement in the force-time history correlation (blue long dashed line in Figure 7), the initial oscillations in the force-time history still notably deviated from the experimental results and the predictions made using the conventional shell elements and the finite-thickness cohesive elements. The blocked-ply stacking sequence of the thermoset panel had only six damageable interfaces compared to the 22 damageable interfaces in the thermoplastic panel. These additional interfaces resulted in more mass being added to the thermoplastic panel models with zero-thickness cohesive elements, explaining their increased sensitivity to the representation of the interfaces.

The damage state predicted by the analysis with finite-thickness cohesive elements for the thermoplastic panel and the corresponding UT amplitude plots are presented in Figure 8. Unlike the thermoset case (Figure 6), the analysis significantly underpredicted the size of the projected through-thickness damage in the UT amplitude plot. Despite the significant changes observed in the predicted force-time histories, none of the interface discretization variations discussed in this section produced a significant change in the predicted damage size.

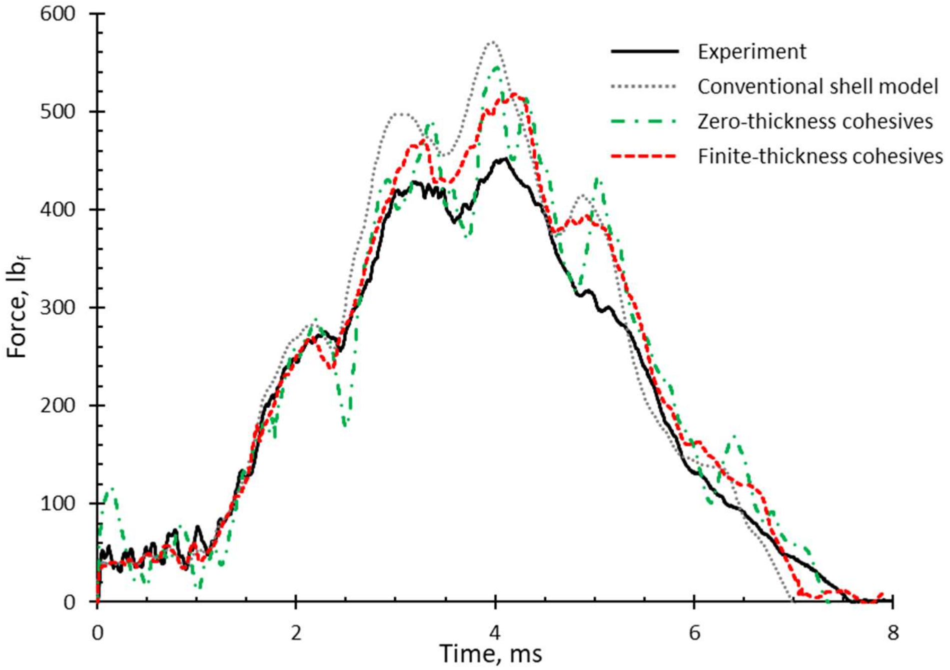

Figure 5. Force-time histories for a 3.5 ft-lb$_f$ impact on a 14-inch thermoset panel using different discretization approaches.

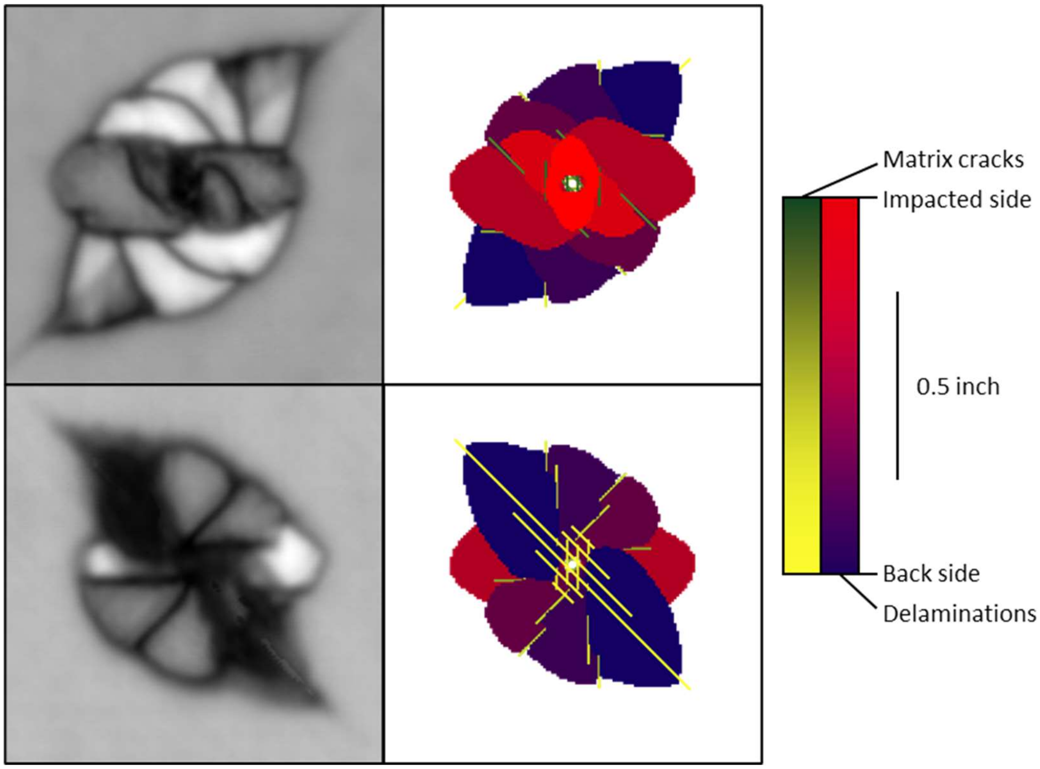

Figure 6. Damage state for a 3.5 ft-lb$_f$ impact on a 14-inch thermoset panel by UT scan (*left*) and PDA with zero-thickness cohesives (*right*), as viewed from the impacted (*top*) and back (*bottom*) sides.

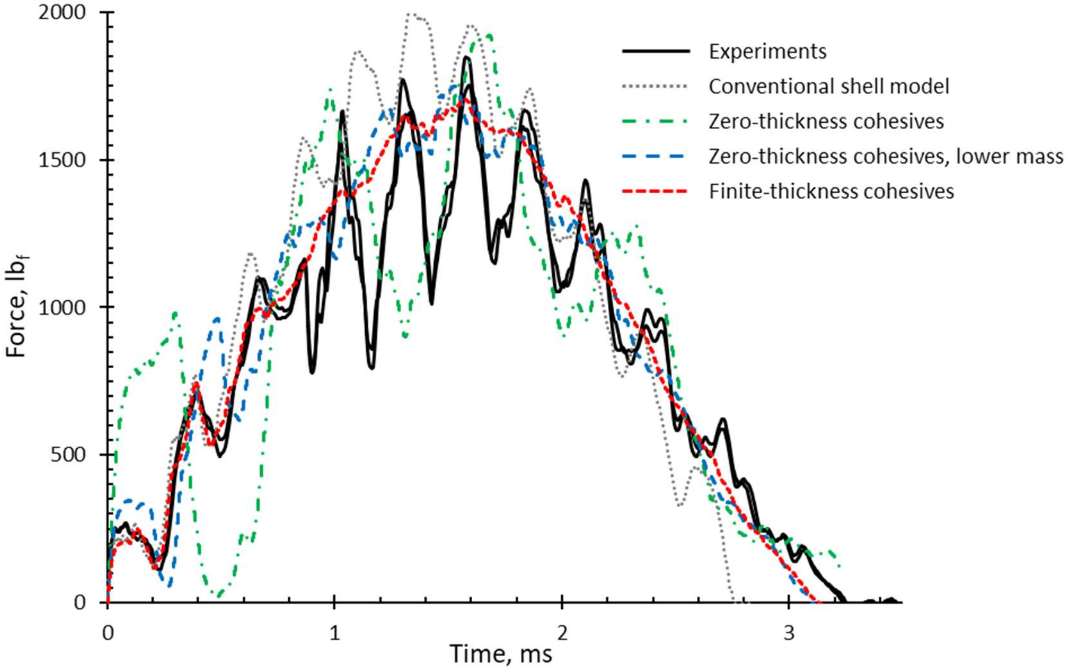

Figure 7. Force-time histories for a 10 ft-lb$_f$ impact on an 8-inch thermoplastic panel using different discretization approaches.

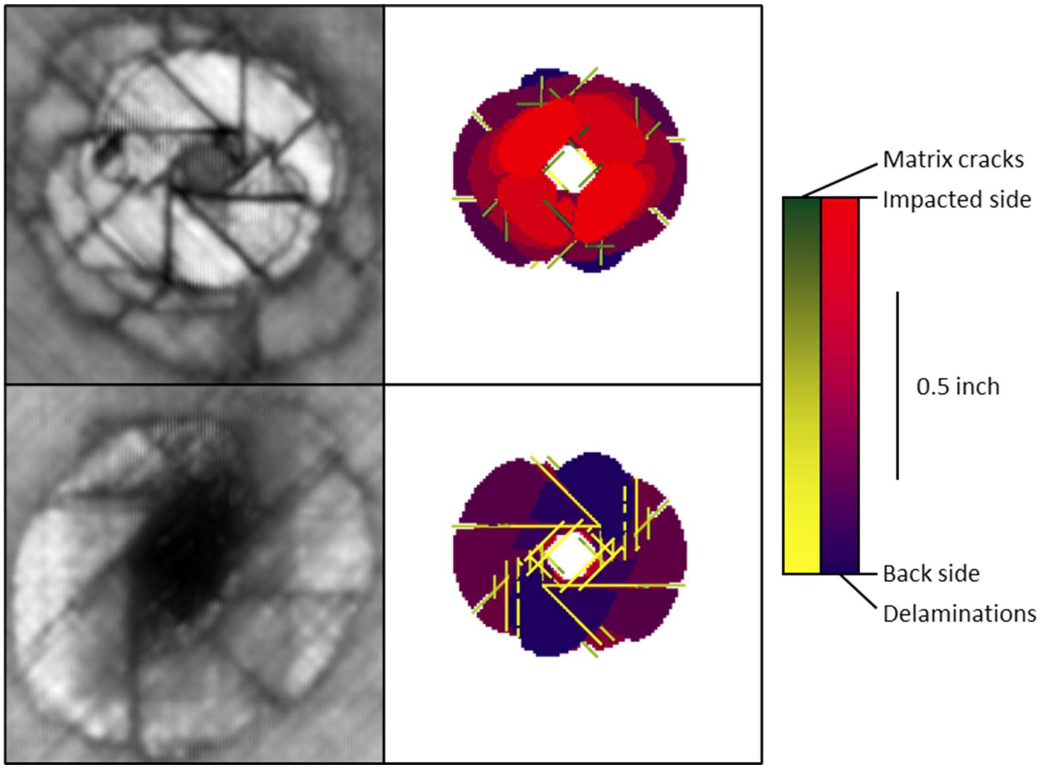

Figure 8. Damage state for a 10 ft-lb$_f$ impact on an 8-inch thermoplastic panel, by UT scan (*left*) and PDA with finite-thickness cohesives (*right*), from the impacted (*top*) and back (*bottom*) sides.

Residual Thermal Stresses

Residual thermal stresses were included in the analyses to promote matrix crack initiation earlier in the impact events. It was hypothesized that by having more matrix cracks present earlier in the damage evolution history, the shape and connectivity of the predicted delaminations may be affected. Wedge-shaped delaminations oriented in a spiral staircase-like pattern (e.g., the bottom-right of Figure 2) are more likely to form when matrix cracks are predicted earlier. Conversely, with fewer instances of matrix cracks in adjacent plies, delaminations are more likely to be elliptically shaped, as can be seen in top-right of Figure 8.

Force-time histories from one experiment and four analyses for a 6 ft-lb$_f$ impact on an 8-inch thermoplastic panel are shown in Figure 9. In the analyses, stress-free temperature differences, ΔT, of 0°F, 100°F, 200°F, and 300°F were used. These analyses used finite-thickness cohesive elements to represent the damageable interfaces and allowed for the prediction of fiber damage, though no fiber damage was predicted in these analyses.

For the range of stress-free temperature differences evaluated, no significant effect on the predicted force-time histories was observed. The experimental and analytical force-time histories agree well in terms of initial stiffness, peak force, and the duration of the impact. The period and amplitude of the vibrations within the responses agree closely until approximately 1.2 ms. At 1.2 ms, a sharp load-drop introduced a higher-frequency component into the experimental force-time history, which was not present in any of the analyses. While tensile fiber damage was not predicted to initiate in any of the residual thermal stress analyses, the failure criterion did reach approximately 98%

at the point of maximum vertical displacement in the 300°F analysis. The experimental load-drop at 1.2 ms in Figure 9 resembles load-drops associated with unstable delamination propagation and possible fiber failure, as will be discussed in the following section.

The fracture energy dissipation histories for the four residual thermal stress analyses were used to study how the dissipated fracture energy per damage mode (i.e., matrix cracking and delamination) varies as a function of stress-free temperature difference. The *fracture energy ratios* for matrix cracks and delaminations in Figure 10 are calculated by dividing the fracture energy dissipation histories by the total dissipated fracture energy in the corresponding $\Delta T = 0°F$ cases. The amount of matrix cracking steadily increased with increasing ΔT, as shown in Figure 11, with the 100°F, 200°F, and 300°F analyses dissipating 1.2, 1.5, and 2.0 times more energy than the 0°F case, respectively. By contrast, the size of the delaminations were virtually unchanged for all evaluated ΔT values, as is shown in terms of dissipated fracture energy in Figure 10 and visually in Figure 12. The delamination morphology only noticeably changed in the 300°F analysis, with only a 4% increase in dissipated fracture energy.

The analytical fracture energy dissipation histories reveal that damage growth occurred during periods of increasing impact force, and predominantly while increasing the impact force beyond its previous maximum value. No significant damage growth was predicted after reaching the peak load. If damage growth in LVI cases grows predominantly at new, higher impact forces, damage predictions should be comparable to those from equivalent static indentation cases (e.g., [10]). In addition, these observations correlate with the uncoupled nature of the force-time and damage size predictions with respect to interface discretization.

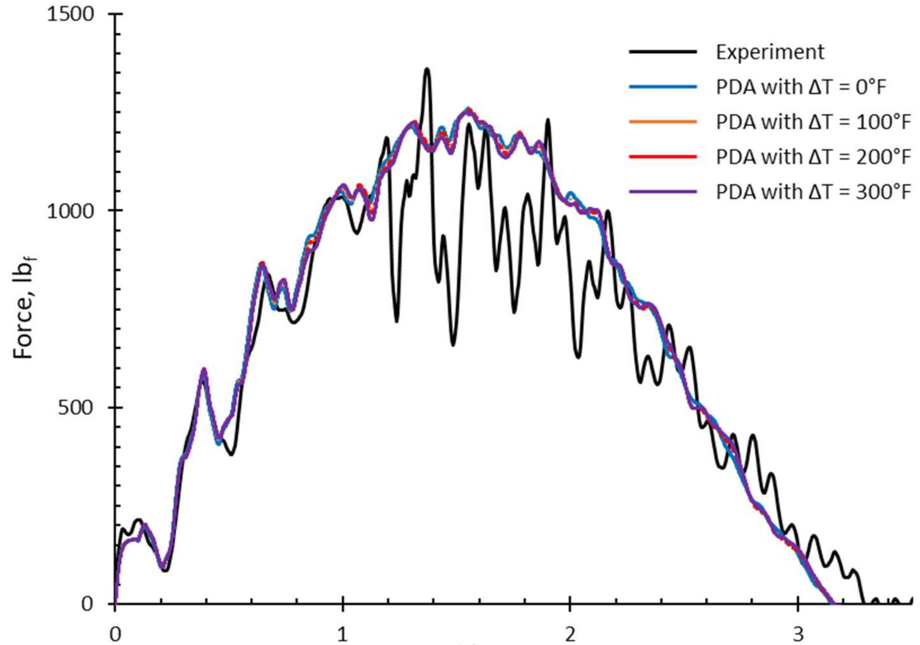

Figure 9. Force-time histories from an experiment and analyses of a 6 ft-lb_f impact on an 8-inch thermoplastic panel with different stress-free temperature values.

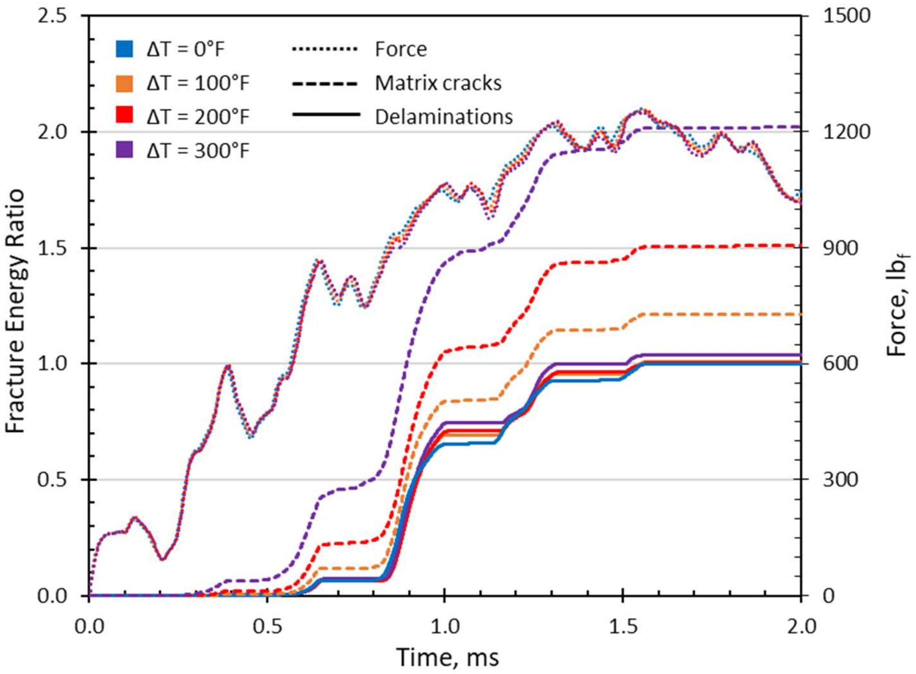

Figure 10. Matrix crack and delamination fracture energy histories for analyses of a 6 ft-lb_f impact on an 8-inch thermoplastic panel with different stress-free temperatures. The *fracture energy ratio* is calculated by dividing the modal fracture energy histories by the final values of the corresponding ΔT = 0°F cases.

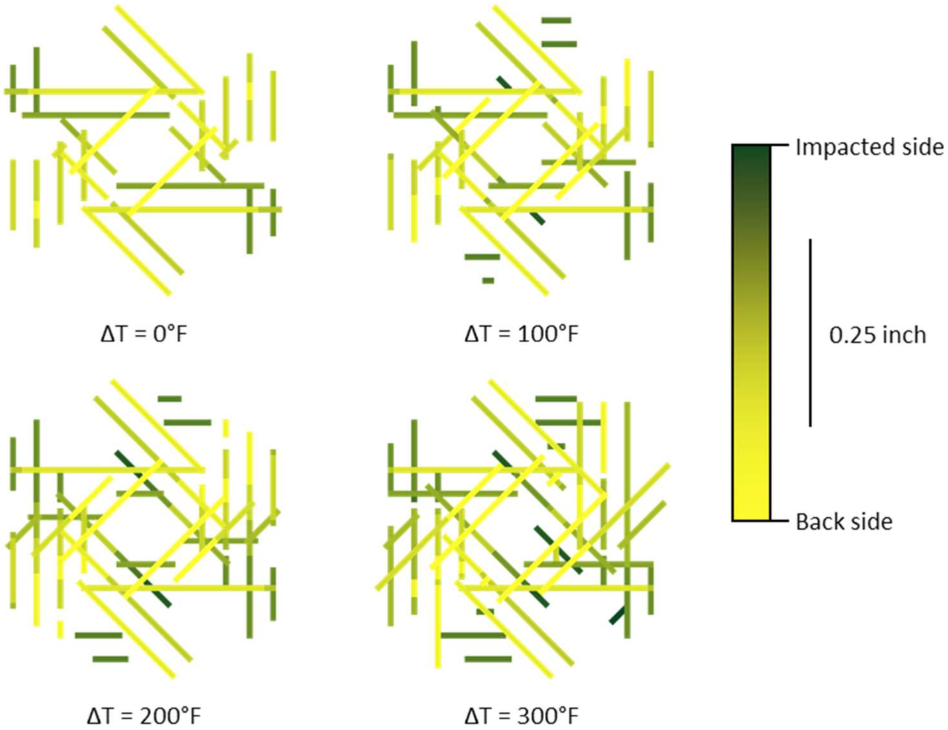

Figure 11. Matrix cracks predicted for a 6 ft-lb_f impact on an 8-inch thermoplastic panel using different stress-free temperatures, as viewed from the back side.

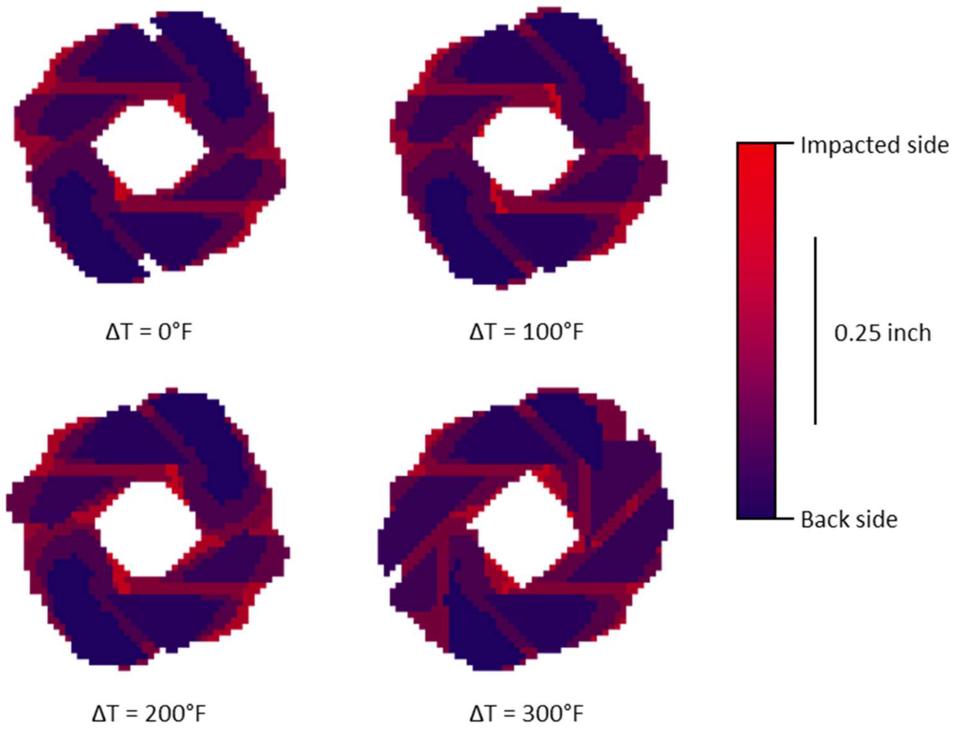

Figure 12. Delaminations predicted for a 6 ft-lb$_f$ impact on an 8-inch thermoplastic panel using different stress-free temperatures, as viewed from the back side.

In summary, the consideration of residual thermal stresses can appreciably affect the amount of predicted matrix cracking. The additional predicted matrix cracking may or may not affect the morphology of predicted delaminations and does not have a considerable effect on the prediction of the overall projected damage size.

Fiber Damage

A conventional CDM approach was used to predict and represent tensile and compressive fiber damage with the CompDam material model. A maximum strain failure criterion was used to define fiber damage onset, and a two-part piecewise linear softening law was used to define the degradation of the material stiffness after onset.

Experimental and analytical force-time histories for a 10 ft-lb$_f$ impact on an 8-inch thermoplastic panel are shown in Figure 13. Two analysis curves are included, one from an analysis with fiber damage disabled (the blue dotted line) and one from an analysis with fiber damage enabled (the red dashed line). Both of the analyses represented in Figure 13 used finite-thickness cohesive elements and included residual thermal stresses with a stress-free temperature difference of 200°F. The two force-time histories are essentially equal until a sudden load-drop occurs at 1.5 ms in the analysis with fiber damaged enabled. This load-drop coincided with elements in the back-side ply having fully-developed fiber damage variables (i.e., having zero fiber-direction stiffness). Fiber damage initiated in the analysis earlier, at approximately 0.85 ms, but had no appreciable effect on the force-time history. The load-drop in the analysis introduced a vibration to the force-time history that resembles a vibration in the experimental results, which started at approximately 0.85 ms. The vibration in the force-time histories for the 10 ft-lb$_f$ impacts in Figure 13 resembles the vibration in the 6 ft-lb$_f$ impact in Figure 9.

The predicted damage states for the fiber-damage-enabled and fiber-damage-disabled analyses are compared to each other and to the projection of the damage area measured with UT in Figure 14. The inclusion of fiber damage significantly increased the amount of matrix cracking, especially on the back-side ply where fiber failure occurred. The back-side interfaces in the fiber-damage analysis also delaminated in the volume underneath the indenter, which had previously been damage-free. The inclusion of fiber damage in the analysis resulted in a 30% increase in dissipated fracture energy for both the matrix cracking and delamination damage modes. While the inclusion of fiber damage did increase the fracture energy dissipated via delamination and the total projected delaminated area, there remained a significant disparity between the experimental and predicted damage sizes, as illustrated by the black dotted outlines of the measured delaminations in Figure 14.

CLOSING REMARKS

Several PDA model features were studied to learn more about their relative importance to damage predictions in LVI analyses in terms of force-time history, damage morphology, and damage size. The model features explored herein included the representation of the damageable interfaces, the consideration of residual thermal stresses, and the inclusion of fiber damage predictions.

It was found that the force-time history and damage size outputs of the analyses were not closely coupled. The predicted force-time histories varied significantly in terms of initial slope and frequency content when changes were made to the damageable interface representation, but no significant changes in the total projected damaged area or the damage morphology were observed. While the force-time histories clearly varied with details of the interface representation, the coarser features of the LVI response (i.e., peak load and impact duration) were relatively constant. Conversely, significant changes in the amount of predicted matrix cracking resulted from varying the stress-free temperature difference in the residual thermal stress analyses, but the predicted force-time histories were virtually unaffected. The prediction of fully-developed fiber damage, however, did introduce an additional vibration to the force-time history and did affect the overall predicted damage size, but the effect on damage size was not significant enough to close the test/analysis correlation gap.

Fracture energy dissipation histories showed that damage growth occurred only when loads increased to new, higher values, suggesting that LVI damage predictions may be comparable to those from equivalent static indentation analyses. As there were no rate-dependent material effects included in the performed analyses, a close equivalence of LVI and static indentation analyses makes sense.

None of the model features explored herein had a significant effect on the apparent interfacial fracture toughness of the impacted thermoplastic panels. Given the remaining considerable gap between the experiments and analyses in terms of total projected damage size, the simplifying assumptions used in the models and the dependencies of pertinent material properties thus far ignored (e.g., interfacial fracture toughness varying with strain rate and/or the direction of delamination propagation with respect to bounding ply orientations) should be revisited.

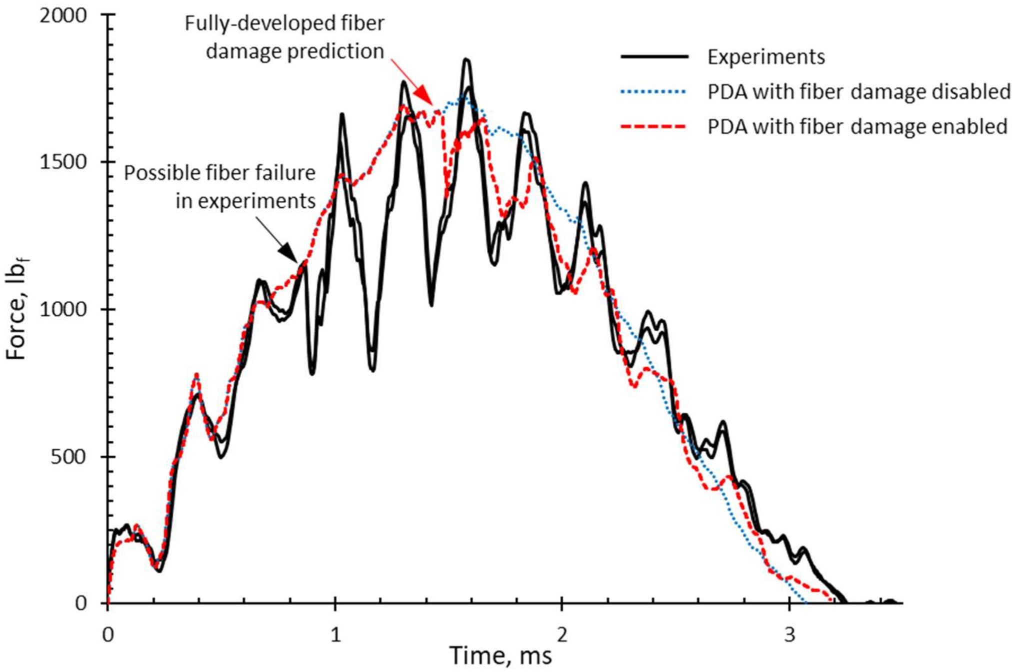

Figure 13. Force-time histories for a 10 ft-lb$_f$ impact on an 8-inch thermoplastic panel for experiments and for analyses with and without fiber damage.

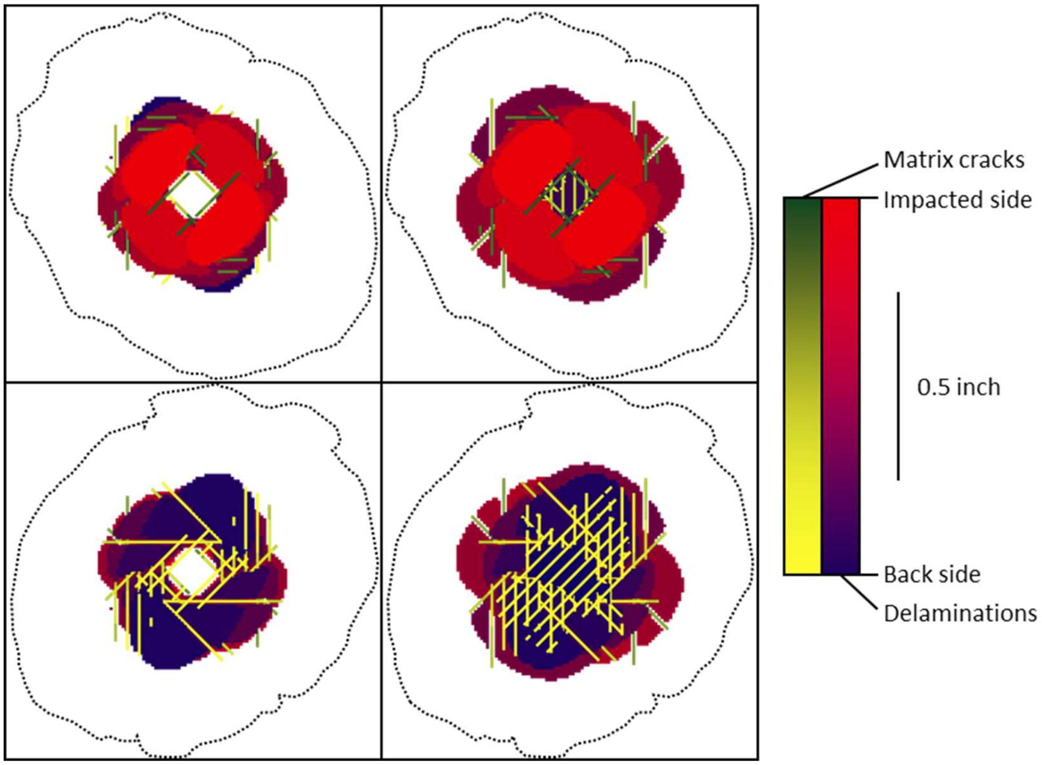

Figure 14. Damage states for a 10 ft-lb$_f$ impact on an 8-inch thermoplastic panel with fiber damage disabled (*left*) and with fiber damage enabled (*right*), as viewed from the impacted (*top*) and back (*bottom*) sides. The dotted lines represent the delaminations determined via UT and X-ray CT.

REFERENCES

1. Wanthal, W., J. Schaefer, B. Justusson, et al. 2017. "Verification & Validation of Progressive Damage/Failure Analysis for Stiffened Composite Structures," *32nd American Society for Composites Technical Conference*, October 23–25, 2017.
2. Leone, F. A., K. Song, W. Johnston, et al. 2019. "Test/Analysis Correlation of Damage States in Post-Buckled Stiffened Validation Building Block Specimens," *34th American Society for Composites Technical Conference*, September 23–25, 2019.
3. Leone, F. A., K. Song, C. A. Rose, et al. 2020. "Progressive Damage Analysis of Post-Buckled Stiffened Panels under Static Compressive Loading," *AIAA SciTech Forum*, January 6–10, 2020.
4. Action, J. and F. A. Leone. 2020. "Progressive Damage Failure Analysis of a Multi-Stringer Post-Buckled Panel," *AIAA SciTech Forum*, January 6–10, 2020.
5. Chen, B. Y., S. T. Pinho, N. V. De Carvalho, et al. 2014. "A Floating Node Method for the Modelling of Discontinuities in Composites," *Engineering Fracture Mechanics*, 127:104–134.
6. Jackson, W. C., C. Rose, and F. Leone. 2023. "Characterization of Low-Velocity Impact Damage in Thermoplastic Laminated Composites," *38th American Society for Composites Technical Conference*, September 18–20, 2023.
7. Leone, F. A., A. C. Bergan, and C. G. Dávila. 2019. "CompDam – Deformation Gradient Decomposition (DGD)," https://github.com/nasa/CompDam_DGD.
8. Hyder, I., F. A. Leone, B. P. Justusson, et al. 2018. "Implementation of a Matrix Crack Spacing Parameter in a Continuum Damage Mechanics Finite Element Model," *33rd American Society for Composites Technical Conference*, September 24–26, 2018.
9. Tijs, B. H. A. H., M. H. J. Doldersum, A. Turon, et al. 2022. "Experimental and Numerical Evaluation of Conduction Welded Thermoplastic Composite Joints," *Composite Structures*, 281:114964.
10. Song, K., F. A. Leone, and C. A. Rose. 2018. "Analysis of Progressive Damage in Cross-Ply and Quasi-Isotropic Panels Subjected to Quasi-Static Indentation," *AIAA SciTech Forum*, January 8–12, 2018.
11. Maimí, P., P. P. Camanho, J.-A. Mayugo, et al. 2006. "A Thermodynamically Consistent Damage Model for Advanced Composites," NASA/TM-2006-214282.
12. Leone, F. A., C. G. Dávila, G. E. Mabson, et al. 2017. "Fracture-Based Mesh Size Requirements for Matrix Cracks in Continuum Damage Mechanics Models," *AIAA SciTech Forum*, January 9–13, 2017.
13. Bergan, A. C. 2019. "Computational Performance of Progressive Damage Analysis of Composite Laminates using Abaqus/Explicit with 16 to 512 CPU Cores," NASA/TM-2019-220251.
14. Sarrado, C., F. A. Leone, and A. Turon. 2016. "Finite-Thickness Cohesive Elements for Modeling Thick Adhesives," *Engineering Fracture Mechanics*, 168:105–113.